Optimal Mission Planning for Fixed-Wing UAVs with Electro-Thermal Icing Protection and Hybrid-Electric Power Systems

Edvard Frimann Løes Narum[1†], Richard Hann[1], Tor Arne Johansen[1]

***Abstract*— Harsh weather conditions such as wind and icing are severe debilitators to the operations of unmanned aerial vehicles in terms of performance, safety and reliability. Forecasts of atmospheric parameters in the mission area can open many options in terms of how to best traverse said environment. The use of hybrid electric propulsion systems in such vehicles significantly alter operational flexibility and range, and subsequently the versatility of the platform, but they are equally vulnerable to atmospheric conditions. This work will show that taking meteorological forecasts into account when performing path planning optimization on such a platform can lead to improvements in energy efficiency of up to 43%, or reduce the flight time between two points by up to 42%, when compared to a standard, straight cruising flight.**

I. Introduction

Unmanned aerial vehicles (UAVs) have seen a surge in development and research over the past few years, in large part thanks to the versatility of UAVs as survey or transportation platforms. Two major limiting factors in practical UAV operations beyond visual line of sight (BVLOS) are restrictions to the effective range, and challenging weather conditions.

Atmospheric winds and icing conditions are the main hazards considered in this research, and developing ways of safely and efficiently operating in such environments can expand the domain in which UAVs can be operated BVLOS. Winds often constitute significant portions of an aircraft's airspeed, and the inclusion of horizontal wind maps in path planning optimization has been shown to lower both flight times and energy expenditure [1]. Vertical wind is essential for the studies of primarily soaring flight and sailplanes, and research has been done into optimal flight in rising air [2].

Icing conditions are considered detrimental to safe operation, but research on stability and operations in such conditions has increased the last few years [3], [4], [5]. The advent of advanced icing protection systems (IPS) [6] has made it possible to mitigate airframe icing at the cost of energy. UAVs equipped with an electro-thermal IPS will be considered in this work. Such systems apply electric heating to exposed surfaces such as the leading edge of wings in order to actively prevent or remove icing, [7], [8]. Due to the high electric power demands for IPS, a hybrid electric UAV (HEUAV) is considered. Installing a hybrid electric power system (HEPS) mitigates the low specific energy of the battery by adding energy rich fuel that can be used to recharge the battery cells during operation. The system will still benefit from the high available power from the battery, thus enabling the use of electro-thermal IPS that have high peak electric power loads without having to increase the size of the vehicle. HEUAVs are in their relative infancy, but are emerging as promising alternatives to established technologies [9], and can typically provide upwards of a five-fold increase in flight-time compared to a purely electric UAV, at a modest cost to system weight.

As autonomy in UAV operations has expanded over the past few years, so has research in path planning optimization. A multi-objective evolutionary algorithm to minimize fuel expenditure given mission constraints was employed in [10]. Subsequently, the same work implements an ideal operating line control of a thoroughly modelled hybrid electric propulsion system. The current work builds on [1] and [11] which concerns performance optimization of fixed-wing electric UAVs in winds and icing conditions through path planning methods.

The overarching objective of the following research is developing algorithms for optimal path planning of a HEUAV with electro-thermal IPS given meteorological forecasts as input data. To realize this, a sufficiently accurate performance model of the hybrid electric power-train and the aircraft must be available, where the system should be flexible enough to be employed with minimal effort to different platform configurations. The main contributions of the present paper, when compared to [1] and [11], is that vertical winds and HEUAVs (rather than electric) are considered. In addition, there are various improvements in the models and algorithms that improve the performance of the system.

Optimization using particle swarm optimization (PSO) will be made both with respect to energy consumption, and to overall time usage. To demonstrate the potential savings in these regards, the algorithm will be tested on multiple simulated data sets with varying severity in weather conditions, on a realistic HEUAV configuration. Further, the results will be discussed, and an outline of future work will be given, to improve on realism, and reach a system that could feasibly be deployed in the field.

II. Atmospheric weather modeling

To ascertain the efficiency of a given path, an accurate model of different atmospheric parameters at the relevant time and geographical area is needed. In this paper, the calculations are made possible by meteorological data provided by the Norwegian Meteorological Institute as described below.

[1]Center for Autonomous Marine Operations and Systems, Department of Engineering Cybernetics, Norwegian University of Science and Technology, 7491 Trondheim, Norway

[†]Corresponding author · edvard@narum.org

A. Barometric pressure and air density

Atmospheric pressure has significant effects on the induced drag, lift, ice accumulation and general performance of an aircraft. The pressure p is estimated in Pa through the International Standard Atmosphere (ISA) barometric formula, which relates height over sea level h to pressure by

$$p(h) = P_0 \cdot \left(\frac{T_0}{T_0 + L_0 \cdot h} \right)^{\frac{g \cdot M}{R \cdot L_0}} \tag{1}$$

where P_0 is the static sea level pressure of 101325 Pa, T_0 is the sea level standard temperature of 288.15 K, L_0 is the standard temperature lapse rate which is around -0.0065 K/m within 11000 meters of altitude, R is the universal gas constant of 8.3144598 J/mol·K, g is the gravitational acceleration and M is the molar mass of air at 0.0289644 kg/mol.

Also playing a major role in the aerodynamic forces on the vehicle is the air density ρ in kg/m^3. The density is calculated by the ideal gas law and varies with surrounding temperature T and pressure p

$$\rho(T, p) = \frac{M \cdot p}{R \cdot T} \tag{2}$$

where temperature T has unit K.

B. Icing conditions

Icing conditions are combinations of atmospheric conditions that lead to the accumulation of ice on an unheated structure. The formation of ice on the wings of a UAV occurs through exposure to super-cooled liquid droplets, and can be critical to operations. Initially, an increase in drag and subsequent decrease in lift occurs, as the air flow separates from the wings at lower angles of attack. Ultimately, this may lead to stalling and crashing the UAV, and has therefore recently become an area of study for UAV operations in colder climates [5]. Multiple parameters have an effect on icing on an airframe, including velocity, droplet size, liquid water content (LWC), and temperature. In this work, an aircraft is considered to be in icing conditions when operating in a temperature below 0°C, an LWC above 0.01 g/m^3 and experiencing a *relative humidity* above 0.99.

Relative humidity is the ratio of the partial pressure of water vapour e_a to the saturated water vapour pressure at a given temperature e_{sat}. Relative humidity is thus expressed as

$$H(e_a, e_{sat}) = \frac{e_a}{e_{sat}} \tag{3}$$

where e_a in Pa is given by

$$e_a(p, q) = \frac{q \cdot p}{0.622 + 0.378q} \tag{4}$$

where q is the specific humidity, which is ratio of the mass of water vapor to the total mass of the air parcel. The saturated water vapor pressure e_{sat} is dependent on T and is given by

$$e_{sat}(T) = 2 + 10^{\frac{0.7859 + 0.03477(T - 273.16)}{1 + 0.00412(T - 273.16)}} \tag{5}$$

Liquid water content is the measure of the mass of water within a body of air. Specifically, the LWC parameter has unit g/m^3, and can be extracted from the mixing ratio LWC_m in kg/kg by

$$LWC(p, LWC_m, T) = \frac{LWC_m p}{R_d T} \cdot 10^3 \tag{6}$$

where R_d is the specific gas constant for dry air of 287.058 J/kg·K. LWC_m is one of the available meteorological parameters, hence the need for the above conversion.

The water droplet median volume diameter (MVD) in μm, is a measure of the diameter of the average droplet in a body of air, [12]

$$MVD = \left(\frac{3.672 + \mu}{\lambda} \right) \tag{7}$$

where μ is a size distribution shape parameter given by

$$\mu = min\left(15, \frac{1000}{N_c} + 2\right) \tag{8}$$

where N_c is the droplet concentration set to 100 drops/cm^3 as a typical value, but can range upwards of 200 drops/cm^3 in nominal conditions [13]. The slope parameter given by

$$\lambda = \left[\frac{\pi}{6} \rho_w \frac{\Gamma(4 + \mu)}{\Gamma(1 + \mu)} \frac{N_c}{LWC} \right]^{1/3} \tag{9}$$

where ρ_w is the density of water in g/m^3 and Γ is the gamma function.

C. Wind

Wind is one of the primary disturbances in UAV operations, and is a significant factor in energy expenditure and flight times. Given typical wind speeds, flying a stretch in headwind can easily double flight times. For this reason, there are large potential energy, and time, savings by optimizing a path taking geographical wind maps into account. Spatial maps of horizontal wind, separated into east-bound and north-bound maps with magnitudes varying with altitude are available for download. These must be properly interpreted to be of use in the system.

In addition to horizontal wind, vertical wind is also present in most UAV applications. Although the magnitude of vertical wind vectors is lower than that of zonal and meridional wind, the effect of updraft on a UAV can lead to gaining "free" lift, which could play a factor in the calculation of an optimal path. Several factors can lead to vertical wind, such as *ridge lift*, stemming from horizontal wind being deflected upwards after meeting an obstacle such as a cliff face, which is exploited by sailplanes and soaring birds alike. Thermal columns are another potential source of updraft, stemming from pressure differentials as a result of uneven heating of Earth's surface [14].

Let V_w^i be the wind speed vector with respect to an inertial north-east-down (NED) frame such that

$$V_w^i = \begin{pmatrix} w_n \\ w_e \\ w_d \end{pmatrix} \tag{10}$$

where w_n and w_e are the north- and east-component of the wind speed vector respectively and w_d is the downwards facing component. The magnitude of the wind vector is then given by

$$V_w = \sqrt{{w_n}^2 + {w_e}^2 + {w_d}^2} \tag{11}$$

D. Meteorological data

Although forecasts would be needed for an operational planning system, historical data are preferred for testing. Historical meteorological data of the Scandinavian peninsula is available through a webapp called THREDDS Data Server hosted by the Norwegian Meteorological Institute (MET). Here, a multitude of weather data from 2016 and onwards is available for download, where one can specify a desired date, time and geographical coverage and receive relevant data in the Network Common Data Form (NetCDF). Fully processed data is currently available at 3 hour intervals, i.e. at 00, 03, 06, etc. UTC and can be specified freely for the desired area and altitudes. The service also provides a subset of parameters hourly, but these are not archived and will therefore have to be downloaded by the user within 24 hours of being processed.

Relevant to this application are the following downloaded maps and parameters. Two separate three-dimensional wind maps, detailing horizontal wind, indicate longitudinal and lateral wind. They are structured as a cube matrix, where each slice indicates a certain altitude, and the maximum and minimum altitude can be specified before downloading. Another wind map, detailing upwards wind, stored in the same format as the horizontal maps, is also acquired. To get a map of the relative humidity, a map of the spatial temperature, pressure based on altitude and a map of the specific humidity is downloaded. A map of the LWC_m is also available and necessary for evaluating icing conditions and penalties. The maps are indexed with matrices associating values of latitudes and longitudes to cells in the map matrix. All the mentioned data is provided with a zonal and meridional resolution of 2,5 km while the resolution of the vertical slices are roughly 100 m, but decreasing with increasing altitude. Assuming constant and evenly distributed parameters throughout every cell is a simplification, but one deemed necessary.

The Norwegian Mapping Authority supplies a number of detailed maps in different categories for the Norwegian peninsula. Included are *digital terrain models* (DTM) that illustrate elevation at a set resolution for a specified geographical area. For this application DTM maps for sections of the Universal Transverse Mercator (UTM) zone 33N were downloaded at a resolution of 10 m, but later further downscaled to 200 m for computational and practical purposes. The data can be downloaded as a Web Coverage Service (WCS) most easily done by using a given WCS URL in a dedicated program such as QGIS.

III. Aircraft performance model

A mathematical model of the aircraft is essential for determining and improving operational performance. Following is an overview of the relevant equations to express the UAVs performance in terms of aerodynamic forces and moments as well as equations of motion. Many of the following equations of motion follow [15].

A. Equations of motion and power estimation

To efficiently and iteratively create trajectories to be used in the optimization algorithm, it is desirable to specify a minimal amount of independent variables for each discretization step that can be used to seed the more detailed parameters that will be used for power and performance calculations. Four parameters will be used as input data, and since all necessary weather data is obtained independently, one can subsequently calculate a range of useful parameters that follow these four discrete values. The four input parameters are the *flight path angle* γ, two coordinates to indicate the horizontal position of a step and the *airspeed* V_a.

All aerodynamic forces acting on an aircraft are directly proportional to the vehicle's V_a. Airspeed is a measure of the aircraft's velocity relative to the surrounding air, and is a combination of the vehicle's *ground velocity* vector V_g^i and the surrounding wind velocity vector V_w^i, given in an earth-fixed inertial frame by

$$V_a^i = V_g^i - V_w^i \tag{12}$$

where V_g^i is the vector describing the UAV's motion with respect to the ground below, V_a^i describes the projections of the UAV's relative air velocity vector into the same NED frame, and V_a is the magnitude of the vector V_a^i.

Defining γ as the *flight path angle*, which is the angle between the horizontal plane and the ground velocity vector, we can express the time derivative of the UAV's altitude h by

$$\dot{h} = V_g \sin\gamma \tag{13}$$

where V_g is the magnitude of the ground velocity vector. The flight path angle γ will be one of the optimization variables indicating climbing or descending along the path. V_g^i can be expressed in element form as

$$V_g^i = V_g \begin{pmatrix} \cos\chi\cos\gamma \\ \sin\chi\cos\gamma \\ -\sin\gamma \end{pmatrix} \tag{14}$$

where χ is the *course over ground* (COG), calculated as the angle with respect to north between two desired discrete positions. The airspeed V_a^i can be expressed similar to V_g^i

$$V_a^i = V_a \begin{pmatrix} \cos\psi\cos\gamma_a \\ \sin\psi\cos\gamma_a \\ -\sin\gamma_a \end{pmatrix} \tag{15}$$

where ψ is the aircraft heading and γ_a is the *air-mass-referenced flight-path angle* defined as the angle from the horizontal plane to the airspeed vector. Eq. (12) can now be rewritten

$$V_a \begin{pmatrix} \cos\psi\cos\gamma_a \\ \sin\psi\cos\gamma_a \\ -\sin\gamma_a \end{pmatrix} = V_g \begin{pmatrix} \cos\chi\cos\gamma \\ \sin\chi\cos\gamma \\ -\sin\gamma \end{pmatrix} - \begin{pmatrix} w_n \\ w_e \\ w_d \end{pmatrix} \tag{16}$$

Squaring the norm of each side of Eq. (16) gives

$$V_g^2 - 2V_g \begin{pmatrix} \cos\chi\cos\gamma \\ \sin\chi\cos\gamma \\ -\sin\gamma \end{pmatrix}^T \begin{pmatrix} w_n \\ w_e \\ w_d \end{pmatrix} + V_w^2 - V_a^2 = 0 \tag{17}$$

which can be solved for V_g to give a measure of the actual ground speed of the aircraft. The horizontal component of V_g can then be used to get a measure of the flight time t_i of a discretized step i

$$t_i = \frac{L_i}{V_g \cos\gamma} \tag{18}$$

where L_i is the horizontal distance between two desired positions. This is then used to calculate altitude changes based on Eq. (13), as well as energy consumption from expended power. From Eq. (16) one can also obtain

$$\gamma_a = \arcsin\left(\frac{V_g \sin\gamma + w_d}{V_a}\right) \tag{19}$$

Simulations performed in [16] relate the angle of attack α to corresponding aerodynamic lift and drag coefficients C_L and C_D for a 2D RG-15 airfoil, whose relation is used in this work. The generated lift force by the airfoil will be assumed to counteract the weight of the aircraft during flight, and scaled by γ_a, to maintain linearity. The required lift coefficient of a step is then calculated as

$$C_L = \frac{2mg\cos\gamma_a}{\rho S V_a^2} \tag{20}$$

This coefficient value gives a corresponding angle of attack and drag coefficient by performing linear interpolations between values obtained from the authors of [16]. The resultant aerodynamic drag force can then be obtained as

$$F_{drag} = \frac{1}{2}\rho V_a^2 S C_D \tag{21}$$

The propulsion system will have to overcome this drag force as well as the pitch-adjusted gravitational force. The required thrust T_{prop} in Newtons is then given by

$$T_{prop} = F_{drag} + mg \cdot \sin(\gamma_a + \alpha) \tag{22}$$

The required propulsive power in W is proportional to the required thrust and the desired airspeed, expressed as

$$P_{prop}(T_{prop}, V_a) = T_{prop} V_a \tag{23}$$

Further assuming perfect power transmission from the battery or the rectifier to the electric motor (EM), the work in Ws becomes

$$W_s = P_{EM} \cdot t_i = \frac{P_{prop}}{\eta_{prop}} \cdot t_i \tag{24}$$

for some duration t_i in s, where η_{prop} is the propeller efficiency, which is a measure of the ratio of the power applied to the EM and the resulting propulsive power. This model assumes constant power over the time step, which is a necessary simplification due to the complexity of the calculations and length of the path.

B. Icing protection system

As the operational domain in the simulations of this work concern icing conditions, the UAV is assumed to be equipped with an electro-thermal IPS such as [7], [8]. An IPS typically works by predicting or detecting icing conditions during operations and then employing mitigating actions. This is done by activating electro-thermal panels installed on the airframe either melting the ice (de-icing mode), or preventing ice from forming (anti-icing mode).

In regards to icing, two factors play heavily into the in-flight performance estimations; power consumption from the IPS, and the increased drag coefficient as a result of icing on the airframe. Two separate algorithms, one for de-icing loads, and one for anti-icing loads, are outputting power loads P_{IPS} based on

$$P_{IPS}(V_a, LWC, T) \tag{25}$$

where V_a, LWC and T are airspeed, liquid water content and temperature respectively. Determining whether to use de-icing or anti-icing for a given step is done by comparing the sum of required power for anti-icing and operating with an ice-free airframe to the sum of using de-icing and flying with an airframe subjected to a degraded drag model as a result of ice accumulation.

The models of drag performance penalties and IPS power loads must be found specifically for each UAV using (icing) wind tunnel tests or computed using advanced numerical methods. We will get back to this in connection with the case study in section V-A.

C. IPS-free performance degradation and ice accumulation

To illustrate the importance of an IPS during flights in icing conditions, and to investigate the alternatives, it is desirable to employ a model for aerodynamic performance degradation as a result of airframe icing. Together with the data detailing the relationship between angle of attack, C_L and C_D on a clean airframe, [16] also produced the same relationships of the airframe after being exposed to different icing conditions for a set amount of time. The data specifies the resulting degraded lift and drag coefficients from being exposed to icing conditions with specific MVD and temperature values, using different angles of attack. Interpolating between the values allows estimates of performance degradations in different icing conditions. The same study also produced a model for the mass of the ice accumulating on an airframe, which will also be considered during no-IPS flight. These models will be explained in greater detail, and more extensively tested, in [17].

D. Hybrid electric power-train modeling

Hybrid-electric propulsion systems in UAVs is a relatively new concept, pioneered by the Diamond DA36 E-Star in 2011 [18]. Motivation surrounding the development of HEPS for UAVs is primarily increasing operational range without sacrificing the benefits of a smaller aircraft design. As the operational limitations of the vehicles are determined in large by the weight and available power, specific energy

density of the power sources arise as an important factor. Specific energy density refers to the energy per unit mass of a medium, and is typically denoted by Wh/kg.

Most HEPS use a fuel tank feeding an internal combustion engine (ICE) connected either mechanically to the drive-train, or its generated power is converted to electrical energy through a generator. ICE based HEPS typically get their energy from gasoline, having a specific energy of around 13 kWh/kg [19]. Much of this energy will be lost during operation due to inefficiencies in coupling, thermal losses and combustion, but one can still expect significant amounts of energy with relatively small amounts of fuel.

There are multiple HEPS configurations, which are described in detail in [20]. The one assumed in this research is a variant of the series hybrid configuration, where there is no mechanical coupling between the combustion power-train and the battery. Instead, a brushless AC-motor is driven in reverse by the ICE to generate electricity. A rectifier converts the alternating current to direct current, which can drive the EM and subsequently the propeller, or charge the battery.

Combining a battery model and the ICE-driven power generation model, one can simulate the power system. The battery is charged and discharged in the same manner, so the battery capacity at time step i+1 is given by

$$C_{i+1} = C_i - \dot{C}_i(P_i - P_{gen}, C_i) \cdot t_i \tag{26}$$

where $P_i = P_{prop} + P_{IPS}$ is the required power at step i, P_{gen} is the generated power, t_i is the length of the time step and $\dot{C}_i$ is a function describing rate of change of capacity at a certain voltage given a supply or demand in power. $\dot{C}_i(P_i, C_i)$ is designed such that $\dot{C}_i(P_i, C_i) = -\dot{C}_i(-P_i, C_i)$ which implies that the remaining capacity of the vehicle increases if $P_{gen} > P_i$ in Eq. (26). $\dot{C}_i$ is defined by

$$\dot{C}_i = \frac{I_i}{3600} = \frac{P_{tot\,i}}{3600 \cdot V_{oci}} \tag{27}$$

where $P_{tot\,i} = P_i - P_{gen}$ is the total power drawn at step i and V_{oci} is the battery potential voltage at step i.

It is worth noting that more complex models for combustion and power generation processes exist, but due to the large discretization steps in the path planning algorithm, they can be considered relatively constant, as complex behaviors are likely to disappear over longer horizons. This is further justified by the structure of the HEPS, in that it can be driven separately from the EM and the battery, and thus be run at a constant, ideal operating point.

E. Battery modeling

Integral to most modern HEPS is the battery, which has become commonplace in UAVs, whether in a fully electric or hybrid configuration. Not only are there multiple advantages over pure combustion drive-trains in terms of emissions and operational noise, but also that of potential power. What batteries are lacking in terms of energy density compared to aircraft fuel, they make up for in *specific power*, which is the ratio of available power to the weight of a power source in W/kg, and *power density* which is the ratio of power to volume in W/m^3. In practice, this opens up options for the miniaturization of the vehicles, as smaller micro aerial vehicles (MAV) with limited available weight and design space can still supply sufficient power to an EM and electric IPS.

Lithium Polymer (LiPo) battery cells are the most commonly used in UAV applications, with a specific power of up to 430W/kg and a specific energy density of up to 0.22 kWh/l, the highest of the common battery types. In this work the dynamic model of the battery is based on the Tremblay's model from [21] and supplemented by [2]. The main assumptions for this model are

- Constant internal resistance
- Charging and discharging characteristics are each other's reciprocal
- No temperature effects
- No self-discharge
- No memory effects or cycle life

Define

$$\begin{aligned} A &= V_{full} - V_{exp} \\ B &= \frac{3}{C_{exp}} \\ C_r &= C_{cut} - C \end{aligned} \tag{28}$$

where V_{full} is the voltage at maximum capacity, V_{exp} is the voltage at the end of the exponential range of the battery, C is the discharged capacity in Ah, C_{cut} is the discharged capacity at the cut-off limit in Ah. The battery potential V_{oc} in V can then be represented by

$$V_{oc}(C, V_0) = V_0 - \left(\frac{\kappa C_{cut}}{C_r}\right) + Ae^{-BC} \tag{29}$$

where V_0 is defined as

$$V_0(V_{oc}, I_{eff}) = V_{full} + \kappa + R_c \cdot I_{eff} - A \tag{30}$$

where R_c is the constant internal resistance in the battery in Ω and I_{eff} is the effective current in A given by

$$I_{eff} = \frac{P_{eff}}{V_{oc}} \tag{31}$$

using I_{eff} as a variable rather than the constant specified discharge current as in the regular Tremblay model. This is due to the power consumption being considered constant during a discretization step. Further, κ is the polarization voltage in V given by

$$\kappa = \frac{\left(V_{full} - V_{nom} + A(e^{-BC_{nom}} - 1)\right)(C_{cut} - C_{nom})}{C_{nom}} \tag{32}$$

Thus, a nonlinear equation representing V_{oc} is obtained as

$$\begin{aligned} V_{oc}^{n+1} - \left(V_{full} + \kappa - A - \frac{\kappa C_{cut}}{C_r} + Ae^{-BC}\right) V_{oc}^n \\ - R_c I_{rated}^{1-n} P_{eff}^n = 0 \end{aligned} \tag{33}$$

where n is the Peukert's constant for the specific battery, I_{rated} is the rated maximum discharge current for the battery in A. The equation can be solved with a nonlinear solver.

IV. Mission planning

A simulation environment for the meteorological data, UAV model, mission parameters and optimization algorithm was built to quantify the energy and time-wise improvements that could be made. This section will explain the method of optimization, structure of the code base, the used resources and specify the platform configuration for the simulations.

A. Cost functions

To realize the optimization algorithm, a proper cost function is needed. The purpose of the cost function is to quantify the success of a given solution, which can be used in an optimization algorithm to compare alternative solutions and determine the best one. Infeasible solutions are given infinite cost the moment they are deemed infeasible. Solutions are deemed infeasible for infractions such as breaching the highest set altitude (in this case 2300m), going below the topography at any point or reaching the cut-off capacity in the battery.

For energy optimization, a measure of expended energy is required. This is based on the cumulative remaining energy both in terms of battery capacity, and of fuel. The cost function is, with that in mind, expressed as a measure of spent energy in Ah

$$COST_{energy} = C_{cut} - C_{end} + \frac{2(F_{full} - F)\eta_{tot}\rho_{fuel}E_{fuel}}{V_{exp} + V_{nom}} \quad (34)$$

where C_{cut} is the maximum discharged capacity from the battery, C_{end} is the remaining battery capacity at the end of the mission, F_{full} is the initial fuel level, F is the remaining fuel level, η_{tot} is the total efficiency in the system, ρ_{fuel} is the density of fuel, E_{fuel} is the total energy in fuel per kg and V_{exp} and V_{nom} is the voltage at the end of the exponential range and the nominal range respectively. In a physical sense, the last term in Eq. (34) expresses how much battery capacity one could expect to regenerate with the remaining fuel given an average nominal battery voltage. We note that the rationale for energy cost minimization is not the cost of fuel and electric energy itself, but rather that it indirectly maximizes operational range, endurance and safety margins, [22].

In some situations, it is desirable to optimize the time of mission completion rather than expended energy. The cost function is then simply the sum of each time step through a solution. A further complication to this cost function could be to penalize energy expenditure close to the cut-off value, so that one is guaranteed a solution with enough remaining capacity to perform for instance landing maneuvers. However, through simulations, this has not been deemed necessary as most time optimizations have generally caused reduced energy expenditure, as will be shown in Section VI.

B. Particle swarm optimization

The cost function must be expected to be non-convex due to the complexity of the atmospheric models and other non-linearities, and non-smooth due to the use of lookup-tables and maps. We have therefore chosen an optimization algorithm that is designed to handle these challenges, i.e. the *particle swarm optimization* method, [23]. PSO is based on the concept of *swarm intelligence* which is accumulating knowledge or learning from decentralised, self-organised systems [24]. Generally, the optimization works by randomizing a population of *particles*, which is a quantifiable candidate solution to the optimization problem. These particles move iteratively and semi-randomly through the viable search-space through a changing *particle velocity* which indicates the direction in which a better solution might be found.

The aforementioned particles are in essence relatively simple suggestions of a potential path, designed to seed a more detailed solution. Each particle contains separate vectors of waypoint positions in an east-north-up (ENU) frame, desired airspeeds and climbing angles. Each particle has an associated particle velocity which has vectors of similar sizes and physical properties, but these values instead indicate how much each of the particle vectors should be updated in an iteration.

After initializing the world-, mission- and UAV-model, the PSO algorithm is started. To begin with, a generic baseline solution is generated through a particle swarm that is specifically chosen. In this initial solution for a transit mission, the aircraft begins by climbing up to a feasible height, then maintains this height flying straight towards the desired ending point at a constant airspeed, before descending to the appropriate final altitude. The reasons for this baseline solution is twofold. It yields a viable initial solution to push the particles towards feasible solutions in the first, very random steps, and it serves as a quantifiable measure of improvement after the optimization is complete. We note that a similar procedure can be made using the same basic steps, also for more complex missions than transit.

Further, a number of particles (given by a set population size) are randomly generated within the confounds of the mission space, and their associated solutions and costs are calculated. All property vectors of all particles (including the initial generic solution) are then updated every iteration with a change given by the associated particle velocities

$$\begin{aligned} W_x &\leftarrow W_x + W_x^{vel} \\ W_y &\leftarrow W_y + W_y^{vel} \\ A &\leftarrow A + A^{vel} \\ \Gamma &\leftarrow \Gamma + \Gamma^{vel} \end{aligned} \quad (35)$$

where W_x and W_y are the vectors containing the x and y components of ENU way-points W, A is the vector of air-speeds and Γ is the vector of flight path angles. After an update, the particles are constrained to fit within the predefined confounds of the state-space. Prior to the above operation, the particle velocities are updated by

$$\begin{aligned} W_x^{vel} &= w \cdot W_x^{vel} + c_1 \cdot r_1 \cdot (W_{x,cb} - W_x) + c_2 \cdot r_2 \cdot (W_{x,gb} - W_x) \\ W_y^{vel} &= w \cdot W_y^{vel} + c_1 \cdot r_1 \cdot (W_{y,cb} - W_y) + c_2 \cdot r_2 \cdot (W_{y,gb} - W_y) \\ A^{vel} &= w \cdot A^{vel} + c_1 \cdot r_1 \cdot (A_{cb} - A) + c_2 \cdot r_2 \cdot (A_{gb} - A) \\ \Gamma^{vel} &= w \cdot \Gamma^{vel} + c_1 \cdot r_1 \cdot (\Gamma_{cb} - \Gamma) + c_2 \cdot r_2 \cdot (\Gamma_{gb} - \Gamma) \end{aligned} \quad (36)$$

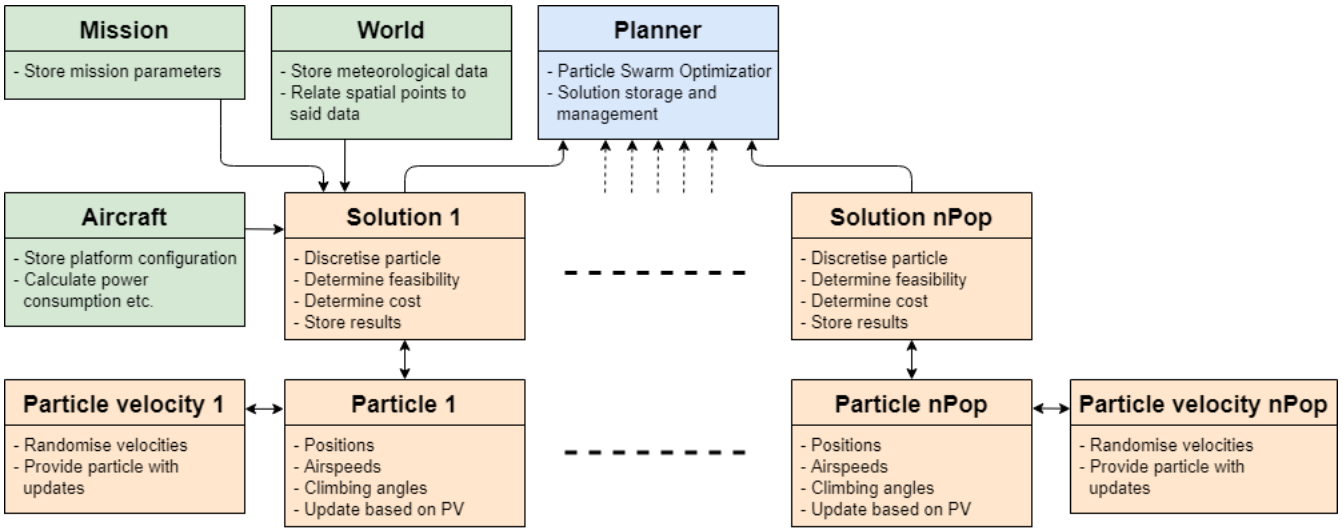

Fig. 1. Software structure

Eq. (36) indicates changes in velocity based on current states as well as local and global current best solutions. Vectors with subscripts *cb* or *gb* indicate the values of the best local and global particle respectively. Local best means the best value the current particle has reached historically while global best is the single best particle value that any solution has been valued at. c_1 and c_2 are tuneable parameters that change how desirable it is to learn from local and global bests respectively, while r_1 and r_2 are randomly generated positive vectors of appropriate dimensions, and are regenerated every iteration for every particle. Finally, w indicates the inertial weight of the particle, which affects how the particle searches for solutions. The initial inertial value is set to 1, encouraging larger searches, but $0 < w \leq 1$ then linearly decreases through the iterations, to let all particles converge towards well-established solutions and focuses the searches more locally.

If a particle reaches the pre-defined spatial domain-limits, a *velocity mirroring* is performed. This is done by mirroring the particle velocity vector to face the opposite direction, which would imply that the particle is moving away from the limit it just reached, and back into the appropriate search space.

C. Algorithm structure

The system was constructed in an object-oriented manner in C++ for reasons of running time, modularity and accessibility in structure. A flow chart of the structure of the software can be seen in Figure 1.

Planner is the central module and can be considered the ”main” function of the system. From Planner, a *Mission* is created with specified parameters. Further it spawns a *World* object, which reads the relevant meteorological data from a data source and stores this in spatial matrix form with read-only member functions to extract the relevant parameters at run-time. An *Aircraft* model is created, which keeps track of platform parameters such as physical constraints, power-train specifications and functions to calculate power requirements and energy consumption at given time intervals.

Planner then initializes as many *Solutions* as the specified population size, each with their own *Particle*. Solutions keep track of simulation results for each Particle at a single iteration, through information such as remaining fuel, battery capacity, altitudes, time expenditure, etc. Particles have specified ENU-frame positions, velocities and climbing angles, which are updated every iteration based on its own Particle Velocity. A copy of the globally best particle and solution, as well as a list of the historically best particles for each member in the population, is kept track of in Planner to properly update the Particle Velocities.

V. Example

A. UAV

To generate quantifiable results and simulations, the configuration of a fixed-wing UAS was applied to the algorithm. In this case study we use the *PX-31* by *Maritime Robotics*, illustrated in Figure 2, which is designed with harsh maritime and arctic environment in mind. With battery power, the vehicle has an empty weight of 15kg, intended for a max take-off weight (MTOW) of 22 kg. The intended cruise velocity of the aircraft is 25 m/s, with a minimum velocity of 14 m/s and maximum of 40 m/s, [22].

The ICE is a 2,5 hp carburettor engine, corresponding to a maximum output power of 1860 W. Desired output power from the generator is around 1 kW to drive the propeller and slowly charge the battery during cruise in normal conditions. With an efficiency in the generator of η_{gen} = 80%, and the efficiency in the ICE of η_{ice} = 15%, the HEPS would have a fuel expenditure of around 0.65 kg/h, based on the specific energy of fuel discussed above. This would give the entire combustion power-train an efficiency of $\eta_{gen} \cdot \eta_{ice} =$ 12%, which is reasonable. The propeller efficiency η_{prop} is considered to be constant at 50 %.

Using a 4000 cc fuel tank, corresponding to around 3 kg of fuel at take-off plus an additional 0.5 kg for the actual

Fig. 2. PX-31 fixed-wing UAV.

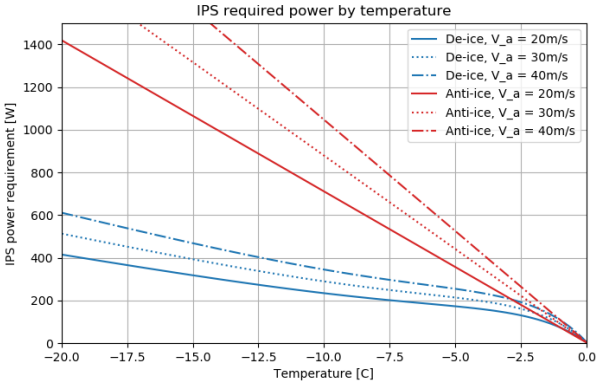

Fig. 3. Power requirements for IPS under different conditions, LWC = 0.4 g/m^3

weight of the tank as well as 2 kg for the ICE and generator would leave the total weight of the platform 20.5 kg, leaving 1.5 kg for the payload.

The battery parameters are based on a 10-cell LiPo battery, considered to be fully charged during mission start. The battery has parameters C_{cut} = 26.400 Ah, C_{exp} = 2.640 Ah, C_{nom} = 20.400 Ah, V_{full} = 41.8 V, V_{exp} = 39.67 V, V_{nom} = 37.67 V, R_c = 0.015 Ω, I_{rated} = 660 A and n = 1.05.

Power requirement loads P_{IPS} for de- and anti-icing loads are an adaption of [25]. In our simulations, they are determined explicitly in kW by

$$P_{deice} = (-0.7551 \cdot T - 0.1122) \cdot (0.0211 \cdot V_a + 0.4722) \cdot (0.1211 \cdot LWC + 0.9596) \cdot (1.3277 - 1.0366 \cdot (1 - e^{0.3260 \cdot T})) \cdot A$$

$$P_{antiice} = (-0.7551 \cdot T - 0.1122) \cdot (0.0211 \cdot V_a + 0.4722) \cdot (0.1211 \cdot LWC + 0.9596) \cdot A$$

where T is in °C, LWC in g/m^3 and A is the heat surface area set to 0.05 m times the wingspan of 2.1 m.

Curves representing the required power of the IPS in Watts, varying with airspeed and temperature can be seen in Fig. 3. Here, the LWC is considered constant at 0.4 g/m^3 as a reasonable icing condition. The model is created using experimental data between -10°C and 0°C, but shown for temperatures above -20°C, so the power requirements for colder temperatures are assumptions.

Performance penalties when experiencing airfoil icing were estimated in [11] through the simulation tool FENSAP-ICE. Following computation of the drag coefficient C_D in nominal conditions, essential for calculations of required power, it is further altered when experiencing airframe icing through

$$C_D(C_D^0, LWC) = C_D^0 \cdot (0.0785 \cdot LWC + 1.4973) \quad (37)$$

when using de-icing instead of anti-icing, which would leave the drag coefficient unaltered in icing conditions.

B. Mission

Here, four distinct mission profiles will be simulated, on two separate data sets. Firstly, flights between the cities of Bodø and Tromsø will be considered. This route is distinguished as a coastal route traversing highly mountainous terrain. The second is between the two northern cities of Kirkenes and Tromsø, located on the same latitude but roughly 430 km apart. Due to less-than-ideal infrastructure connecting the two cities, travelling the distance by car would take north of 10 hours.

VI. Results

Results from four simulated scenarios are presented in Table I. Profile 1 and 2 are results from February 14. from Tromsø to Bodø and Bodø to Tromsø respectively. Profile 3 and 4 are from February 10., indicating routes from Kirkenes to Tromsø and Tromsø to Kirkenes respectively.

The default solution in all profiles is a straight line at an appropriate altitude based on maximum elevation of the topography below. The default solutions of Profile 1 and 2 require a higher cruise altitude due to the more mountainous terrain below. All default solutions were simulated using a constant desired airspeed of 28 m/s, which is slightly higher than the stated cruise velocity of the PX-31 of 25 m/s. This is to remove some of the inflation in time and energy optimization that stems from just increasing the airspeed across all steps.

Profile 1 saw energy savings optimization totalling a reduction of 43.13% in energy expenditure based on Equation (34). Profile 2, being simulated on the same weather data, but in the opposite direction, saw energy savings of 30.69%. In terms of time optimization Profile 1 and 2 saw a decrease in time expenditure of 42.37% and 17.57% respectively.

Profile 3 and 4, belonging to a longer mission profile, saw higher total energy consumption, with optimizations of similar magnitude, at 43.42% and 41.35% respectively. Time optimizations for the same profiles were quantified as 40.62% and 31.57% respectively.

VII. Discussion

It is apparent that the most significant reductions in energy consumption occur when the algorithm is able to avoid icing conditions through path planning, and reduce the overall flight time. Avoiding icing conditions allows the algorithm to run without an active IPS, causing much lower power

Profile	Expended energy	Time spent	Fuel left	Battery cap left	Tot. time in ice	Avg. height	Tot. path length
1 - Default	118.632Ah	6h14m24s	0.265L	20.604Ah	1h18m50s	1320m	328.0km
1 - Energy	67.471Ah	4h15m29s	2.211L	12.965Ah	0h16m49s	1087m	374.8km
1 - Time	69.930Ah	3h35m45s	2.312L	7.463Ah	0h43m48s	1030m	375.3km
2 - Default	47.503Ah	2h15m56s	2.779L	15.771Ah	0h24m55s	1320m	328.0km
2 - Energy	32.924Ah	2h2m27s	3.155L	19.004Ah	0h0m42s	1237m	333.5km
2 - Time	35.986Ah	1h52m3s	3.170L	15.490Ah	0h19m42s	1290m	334.1km
3 - Default	124.758Ah	5h57m15s	0.507L	7.170Ah	3h22m45s	881m	428.5km
3 - Energy	70.590Ah	4h19m55s	1.982L	16.775Ah	0h21m4s	1517m	448.7km
3 - Time	79.146Ah	3h32m9s	1.643L	18.462Ah	1h30m2s	1353m	438.1km
4 - Default	92.614Ah	4h17m24s	1.236L	17.283Ah	2h14m15s	881m	428.5km
4 - Energy	54.314Ah	3h17m5s	2.594L	14.576Ah	0h11m14s	1598m	436.0km
4 - Time	67.412Ah	2h56m9s	2.388L	7.693Ah	1h15m12s	1405m	436.9km

TABLE I
PROFILE 1: TROMSØ - BODØ 14.02, PROFILE 2: BODØ - TROMSØ 14.02
PROFILE 3: KIRKENES - TROMSØ 10.02, PROFILE 4: TROMSØ - KIRKENES 10.02

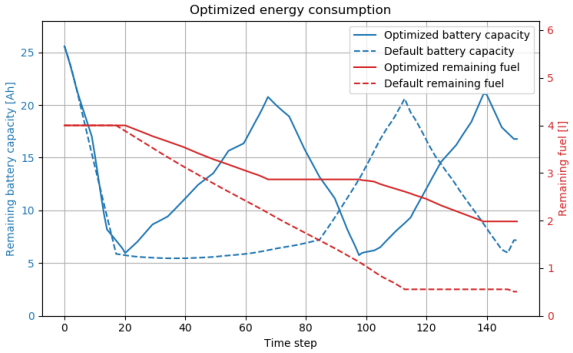

Fig. 4. Default and optimized energy consumption for Profile 3

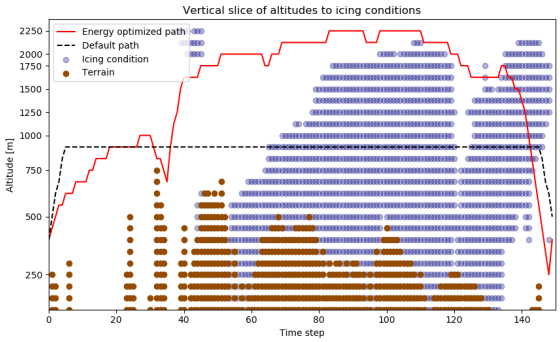

Fig. 5. Altitudes of energy optimized path for Profile 4 relative to icing conditions

consumption. As an example, Profile 3 is estimated to save around 1.5L of fuel through optimization, potentially allowing very meaningful expansions of the mission profile, such as a return flight with the same configuration. Fuel consumption and remaining battery capacity for this profile is shown in Fig. 4. Note the default solution's inability to properly recharge the battery through certain sections, likely stemming from constantly high power requirements from the IPS. Most solutions will prefer higher desired airspeeds through all steps, as the increased power requirements for higher speeds is mitigated by the energy saving associated with a shorter flight time.

Fig. 5 displays the altitudes of the energy optimized path of Profile 4, with the corresponding icing conditions, terrain elevations and default solution altitudes. All icing conditions and terrain displayed belong to the vertical column of the positions corresponding to the optimized path All altitudes are rounded to the closest, discrete cell in the weather data. It is apparent the algorithm generally desires high altitudes, likely due to the lower air pressure, and the subsequently lower power consumption, while still staying out of active icing conditions.

Generally, performing time optimizations also reduce energy expenditure, but more so in unavoidable icing conditions. The magnitudes of time optimizations is, intuitively,

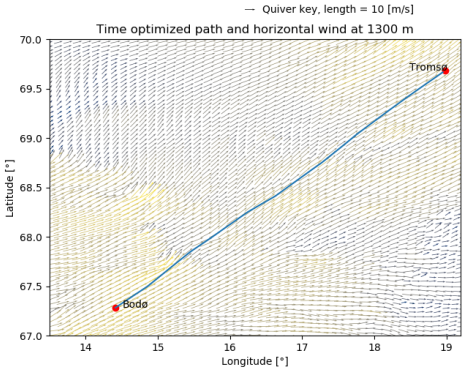

Fig. 6. Time optimized path in relation to horizontal wind at 1300m altitude for Profile 2

dependent on the variations in the wind maps. Through simulations and experimentation, significant reductions in energy consumption by considering vertical wind was not observed. Further savings could feasibly be made by allowing tactics such as energy harvesting through circling flight, as in [2]. A plot of the time optimized path of Profile 2 in relation to the horizontal wind at an altitude of 1300 m can be seen in Fig. 6.

As the power consumption of the de-icing system is typ-

ically significantly less than that of the anti-icing protection system, the degraded drag from experiencing airframe icing is, through simulations, very seldom high enough to favor anti-icing over de-icing. Usage of the anti-icing system could be more favorable when adding penalties to for instance stability when permitting ice accumulation. Further work will have to be done in determining which icing protection strategy should be employed through different steps.

All missions profiles are also attempted on a configuration without an active IPS, using the ice accumulation data from [16]. Generally, the default solutions are unable to finish the routes, quickly draining their batteries. This is due to the increased drag coefficient causing higher power requirements than the HEPS can deliver, never allowing the battery to recharge. Only in Profile 2, taking advantage of the strong tailwind and short total time in icing conditions, is the system able to finish without an IPS. However, performing optimizations on these configurations often achieves similar performance to that of the results presented in Table I, as most of the icing conditions are avoidable through path planning. More detailed results regarding no-IPS flight will be presented in [17].

The simulations presented in this work are currently done on static weather maps, which is somewhat unrealistic. An improvement could be performing an interpolation between consecutive data-sets based on the cumulative time spent at every step, but that is expected to lead to optimizations of similar magnitude as the current version, since the data would still be deterministic. Another interesting experiment could be performing optimizations on weather forecasts, but evaluating based on resulting historical data, which could give an indication of the uncertainty of these optimizations.

VIII. Conclusion

This work has demonstrated the magnitude of the potential operational savings one can achieve by taking spatial weather data into account when performing path planning optimizations for hybrid-electric unmanned aerial vehicles. This was done by using particle swarm optimization with an aircraft model equipped with an icing protection system on historical weather maps. In a practical application, this could serve as a high-level planning system for long-range UAVs operating in wind and icing conditions, limited mainly by the accuracy and resolution of the available weather data.

ACKNOWLEDGMENT

We are grateful to UBIQ Aerospace AS and Maritime Robotics AS for providing some of the data used in the simulations. We thank Fabio Andrade and Anthony Hovenburg for making the software used in [11] available.

The work was supported by the Research Council of Norway and industry partners through the Center for Excellence AMOS grant number 223254, Centre for Integrated Remote Sensing and Forecasting for Arctic Operations (CIRFA) grant number 237906, D-ICE Rotors grant number 296228, FlightSmart grant number 282004, and Regionalt Forskningsfond Midt-Norge grant number 285248.

References

[1] A. Hovenburg, F. A. de Alcantara Andrade, C. Dahlin Rodin, T. Johansen, and R. Storvold, "Inclusion of horizontal wind maps in path planning optimization of UAS," in *International Conference on Unmanned Aircraft Systems, Dallas*, 08 2018.

[2] S. Gudmundsson, "A biomimetic, energy-harvesting, obstacle-avoiding, path-planning algorithm for uavs," Ph.D. dissertation, Embry–Riddle Aeronautical University, 2016.

[3] A. Winter, R. Hann, A. Wenz, K. Gryte, and T. A. Johansen, "Stability of a flying wing uav in icing conditions," in *8th European Conference for Aeronautics and Space Sciences (EUCASS), Madrid*, 2019.

[4] S. Armanini, M. Polak, and J. e. a. Gautrey, "Decision-making for unmanned aerial vehicle operation in icing conditions," 12 2016.

[5] R. Hann, A. W. Wenz, K. Gryte, and T. A. Johansen, "Impact of atmospheric icing on uav aerodynamic performance," in *Workshop on Research, Education and Development of Unmanned Aerial Systems (RED-UAS), Linkoping*, 2017.

[6] A. Shinkafi, C. Lawson, R. Seresinhe, D. Quaglia, and I. Madani, "An intelligent ice protection system for next generation aircraft trajectory optimization," in *29th Congress of the International Council of the Aeronautical Sciences, St. Petersburg*, 09 2014.

[7] K. L. Sørensen and T. A. Johansen, "Flight test results for autonomous icing protection solution for small unmanned aircraft," in *Int. Conf. Unmanned Aircraft Systems, Miami*, 2017.

[8] R. Hann, K. T. Borup, A. Zolich, K. Sørensen, H. Vestad, M. Steinert, and T. A. Johansen, "Experimental investigations of an icing protection system for uavs," in *International Conference on Icing of Aircraft, Engines, and Structures, Minneapolis*, 2019.

[9] J. Sliwinski, A. Gardi, M. Marino, and R. Sabatini, "Hybrid-electric propulsion integration in unmanned aircraft," *Energy*, vol. 140, pp. 1407–1416, 12 2017.

[10] J. Y.-C. Hung, "Investigation of methods for increasing the energy efficiency on unmanned aerial vehicles (UAVs)," Master's thesis, Queensland University of Technology, 2011.

[11] A. Hovenburg, F. A. de Alcantara Andrade, R. Hann, C. Dahlin Rodin, T. Johansen, and R. Storvold, "Long range path planning using an aircraft performance model for battery powered sUAS equipped with icing protection system," *submitted for publication*, 2020.

[12] B. E. K. Nygaard, J. E. Kristjánsson, and L. Makkonen, "Prediction of in-cloud icing conditions at ground level using the wrf model," *American Meteorological Society*, 2011.

[13] J. Wallace and P. Hobbs, *Atmospheric Science: An Introductory Survey*, ser. International Geophysics Series, 2006.

[14] U. D. of Transportation, "Aviation weather advisory circular 00-6b," 2016.

[15] R. W. Beard and T. W. McLain, *Small Unmanned Aircraft: Theory and Practice*. USA: Princeton University Press, 2012.

[16] N. Fajt, R. Hann, and T. Lutz, "The influence of meteorological conditions on the icing performance penalties on a uav airfoil," 2019.

[17] E. F. L. Narum, "Mission planning for fixed-wing uavs in wind and icing conditions," Master's thesis, Norwegian University of Science and Technology, Trondheim, 2020.

[18] "Hybrid powered aircraft in paris," 2011. [Online]. Available: https://www.avweb.com/news/hybrid-powered-aircraft-in-paris/

[19] "Energy density of gasoline," 2003. [Online]. Available: https://hypertextbook.com/facts/2003/ArthurGolnik.shtml

[20] J. Schömann, "Hybrid-electric propulsion systems for small unmanned aircraft," Ph.D. dissertation, Technische Universität München, 2014.

[21] O. Tremblay, L.-A. Dessaint, and A.-I. Dekkiche, "A generic battery model for the dynamic simulation of hybrid electric vehicles," *IEEE*, 2007.

[22] A. Hovenburg, T. A. Johansen, and R. Storvold, "Mission performance trade-offs of battery-powered sUAS," in *Int. Conf. Unmanned Aircraft Systems, Miami*, 2017.

[23] J. Kennedy and R. Eberhart, "Particle swarm optimization," in *Proceedings of ICNN'9Hov175 - International Conference on Neural Networks*, vol. 4, Nov 1995.

[24] G. Beni and J. Wang, "Swarm intelligence in cellular robotic systems," 1993.

[25] R. Hann, A. Enache, M. C. Nielsen, B. N. Stovner, J. van Beeck, T. A. Johansen, and K. T. Borup, "Uav icing: Experimental heat loads for electrothermal anti-icing and de-icing," in *Atmospheric and Space Environments Conference*, 2020.